

Phase Wrapping of Epicyclic Perturbations in the Wobbly Galaxy

Alexander de la Vega^{1,2}, Alice C. Quillen², Jeffrey L. Carlin^{3,4},
Sukanya Chakrabarti⁵ and Elena D’Onghia^{6,7}

¹ *Department of Physics and Astronomy, Johns Hopkins University, Baltimore, MD 21218, USA*

² *Department of Physics and Astronomy, University of Rochester, Rochester, NY 14627, USA*

³ *Department of Physics, Applied Physics and Astronomy, Rensselaer Polytechnic Institute, Troy, NY 12180, USA*

⁴ *Department of Physics and Astronomy, Earlham College, Richmond, IN 47374, USA*

⁵ *School of Physics and Astronomy, Rochester Institute of Technology, 84 Lomb Memorial Drive, Rochester, NY 14623*

⁶ *Department of Astronomy, University of Wisconsin-Madison, Madison, WI 53706, USA*

⁷ *Alfred P. Sloan Fellow*

5 March 2022

ABSTRACT

We use test-particle integrations to show that epicyclic motions excited by a pericentre passage of a dwarf galaxy could account for bulk vertical velocity streaming motions recently observed in the Galactic stellar disc near the Sun. We use fixed potential test-particle integrations to isolate the role of phase wrapping of epicyclic perturbations from bending and breathing waves or modes, which require self-gravity to oscillate. Perturbations from a fairly massive Sagittarius dwarf galaxy, $M_d \sim 2.5 \times 10^{10} M_\odot$, are required to account for the size of the observed streaming motions from its orbital pericentre approximately a Gyr ago. A previous passage of the dwarf through the Galactic disc approximately 2.2 Gyr ago (with a then more massive dwarf galaxy) is less effective. If phase wrapping of epicyclic perturbations is responsible for stellar streaming motions in the Galactic disc, then there should be variations in velocity gradients on scales of a few kpc in the vicinity of the Sun.

Keywords: Galaxy: structure – Galaxy: kinematics and dynamics – Galaxy: disc.

1 INTRODUCTION

Significant bulk motions of stars, or streaming velocities, have recently been detected in large scale stellar surveys such as the RAdial Velocity Experiment (RAVE, Steinmetz et al. 2006) and Large Area Multi-Object Spectroscopic Telescope (LAMOST, Cui et al. 2012) radial velocity surveys (Siebert et al. 2011; Williams et al. 2013; Carlin et al. 2013; Xu et al. 2015; Sun et al. 2015). Vertical wavelike structures in the stellar density distribution are also seen in the Sloan Digital Sky Survey (SDSS) data (Widrow et al. 2012; Xu et al. 2015). Curiously, the bulk motions of stars vary as a function of height above the plane, and the vertical bulk motions exhibit patterns of compression and rarefaction. The observed vertical velocity gradients could be due to heating from internal perturbations, such as spiral arms or bars (Faure et al. 2014; Monari et al. 2015), or bending and breathing waves or modes (Widrow et al. 2012; Gómez et al. 2013) that could have been excited by a dwarf galaxy (Widrow et al. 2014). Vertical density and velocity structures arise in simulated Milky Way discs perturbed by a Sagittarius sized dwarf galaxy (Gómez et al. 2013) that could also have

induced warped and ringed structures (such as the Monoceros Ring; Newberg et al. 2002) in the outer Galaxy (e.g., Kazantzidis et al. 2008; Younger et al. 2008; Quillen et al. 2009; Purcell et al. 2011).

Pericentre approaches and passages through the Galactic disc by the Sagittarius dwarf galaxy would have excited both vertical and radial epicyclic motions in stars. A perturbation in the disc could affect a localised region where stars are pushed to the same phase in their epicycles. Over time, these perturbed stars would see a large spread in phases, called phase wrapping, due to the dependence of vertical and radial (epicyclic) oscillation frequencies on orbital angular momentum, eccentricity and inclination (e.g., Minchev et al. 2009), giving spiral and warped structures in the disc (Quillen et al. 2009). However, the perturbation of a dwarf galaxy could also excite vertical bending and breathing waves or modes in the disc (Weinberg 1991; Gómez et al. 2013; Widrow et al. 2014; Widrow & Bonner 2015). N-body simulations would be expected to give a more realistic simulation of perturbations to the Galactic disc caused by the Sagittarius dwarf galaxy. However, with N-body simulations it is difficult to differentiate between excitation of bending or breathing waves or modes from phase wrapping of epicyclic motions. Waves and vibration modes are a property of a self-gravitating disc (Widrow et al. 2012), and so would not be present in a non-interacting test-particle simulation where

particle motions are integrated in a fixed Galactic potential. Here we use test particle integrations to isolate and study the role of epicyclic phase wrapping and explore which structures in the local velocity field might be a result of vertical and radial epicyclic motions excited in the disc by a previous pericentre or a previous passage through the Galactic disc of the Sagittarius dwarf galaxy.

2 TEST-PARTICLE INTEGRATIONS

We integrate particle orbits for two different sets of initial conditions using a fixed gravitational potential for the Milky Way. Particle orbits are integrated using the python library `galpy` (Bovy 2015) using the `MWPotential2014` model gravitational potential. This potential is designed to give a realistic model for the Milky Way and is described in detail by Bovy (2015) in his section 3.5. Our procedure is as follows: We generate a thin disc of 10^7 test particles. We perturb the velocities of each particle, instantaneously approximating perturbations caused by an encounter from a dwarf galaxy. We then integrate the particles to the present day in the static Galaxy potential alone. Each set of integrations required 3–5 days of computations on a Mac-Mini computer with a 2.4 GHz IntelCore 2 Duo processor. The perturbations are applied instantaneously, rather than directly integrated as a function of time, so as to separate between the excitations caused by the perturbations and subsequent phase wrapping in the fixed background Galactic potential.

We consider the role of two perturbations from the dwarf galaxy, separately, so that we can contrast and compare their different roles in exciting epicyclic motions in the stars. We run two separate integrations, one beginning with perturbations caused by the passage of the dwarf galaxy through the Galactic plane approximately 2.2 Gyr ago, and the second integration, beginning with perturbations caused by the dwarf galaxy’s pericentre approximately 1.1 Gyr ago.

We work in the right-handed Galactocentric coordinate system used by Law & Majewski (2010). The relation between Galactic latitude and longitude (on the sky and with origin at the Sun) and the Cartesian Galactocentric coordinate system with origin at the Galactic Center is illustrated in Figure 1. This coordinate system gives a current location of the Sagittarius dwarf at $X, Y, Z = (19.0, 2.7, -6.9)$ in kpc with a distance from the Sun of ~ 28 kpc and Galactocentric solar radius $R_\odot = 8.0$ kpc. In this coordinate system the current location of the Sun is $(-R_\odot, 0, 0)$ and this differs from that used by Carlin et al. (2013) and Sun et al. (2015) who place the Sun at $(R_\odot, 0, 0)$. We also use Galactocentric cylindrical coordinates (R, Θ, Z) , with Galactic rotation $\dot{\Theta} > 0$, and in these the location of the Sun is $(R_\odot, \Theta_\odot, 0)$ with $\Theta_\odot = \pi$, differing from Carlin et al. (2013) and Sun et al. (2015) who adopt $\Theta_\odot = 0$. We work in units of kpc, M_\odot and velocities are given in km s^{-1} . The adopted circular velocity at R_\odot is $V_\odot = 220 \text{ km s}^{-1}$ and the period of Galactic rotation at R_\odot is $P = 2\pi R_\odot / V_\odot = 0.23 \text{ Gyr}$.

2.1 Thin disc prior to perturbation by the dwarf galaxy

Prior to perturbation by a dwarf galaxy encounter, particles are initially evenly distributed in a thin disc. Work-

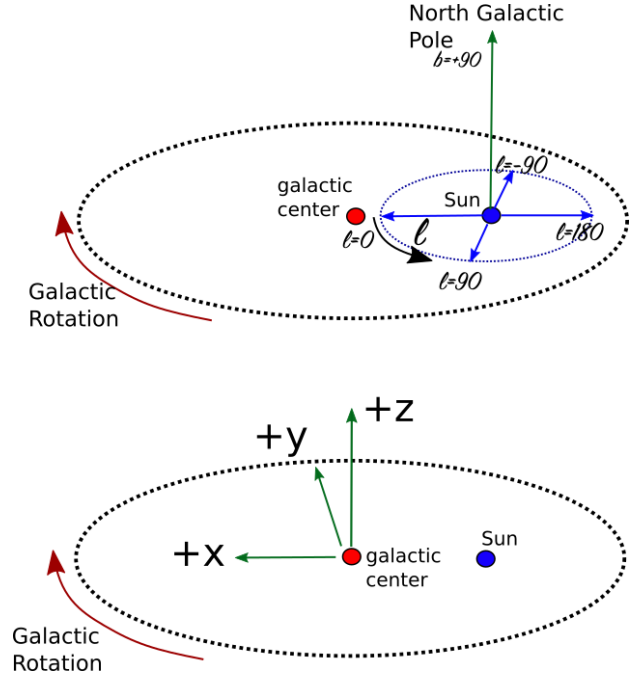


Figure 1. The top panel shows Galactic latitude and longitude (on the sky). The bottom panel shows the Galactocentric cartesian coordinate system.

ing in Galactocentric cylindrical coordinates we start by choosing azimuthal angle, Θ , from a uniform distribution $0 \leq \Theta \leq 2\pi$. Guiding radii are chosen to be uniformly distributed $5 \leq R_g \leq 30$ kpc, giving a surface density proportional to $1/R$. This has a shallower radial gradient than an exponential distribution but allows us to more efficiently study the structure of the outer Galaxy by increasing the number of test particles in that region.

After the guiding radius R_g is chosen, the initial radius, radial and tangential velocity components are chosen using a first order (in radial action variable) epicyclic approximation. The epicyclic amplitudes a_r are chosen to be uniformly distributed between zero and a_{rmax} . Epicyclic angles, ϕ_r , are chosen from a uniform distribution with $0 \leq \phi_r \leq 2\pi$. Initial radii and radial velocities are set to

$$\begin{aligned} R &= a_r \sin(\phi_r) + R_g \\ V_R &= a_r \kappa(R_g) \cos(\phi_r). \end{aligned} \quad (1)$$

The vertical component of the orbit’s angular momentum is $L_Z = R_g V_c(R_g)$ and the initial tangential velocity component computed as $V_\theta = L_Z / R$. Here $V_c(R_g)$ is the rotation curve and $\kappa(R_g)$ is the radial epicyclic frequency, and these are computed using the galactic potential `MWPotential2014` using the `vcirc` and `epifreq` routines from `galpy`. The initial vertical positions and velocities are similarly chosen by choosing an epicyclic amplitude, a_z , uniformly distributed between zero and a_{zmax} , and vertical epicyclic angle ϕ_z , uniformly distributed between zero and 2π , then setting initial Z and vertical velocity component V_Z to be

$$\begin{aligned} Z &= a_z \sin(\phi_z) \\ V_Z &= a_z \nu(R_g) \cos(\phi_z). \end{aligned} \quad (2)$$

Here $\nu(R_g)$ is the vertical oscillation frequency, which is computed in the `MWPotential2014` galactic potential using

the `verticalfreq` routine from `galpy`. Setting $a_{rmax} = 1.6$ kpc and $a_{zmax} = 0.4$ kpc, the resulting disc has velocity dispersions $\sigma_R \approx 20 \text{ km s}^{-1}$, $\sigma_Z \approx 10 \text{ km s}^{-1}$, and $\sigma_\phi \approx 15 \text{ km s}^{-1}$ at $R = R_\odot$ that are consistent with thin disc values computed in the Solar neighbourhood (comparing to Figure 31 by Nordström et al. 2004). The parameters a_{rmax} and a_{zmax} are independent of galactocentric guiding radius, (R_g), corresponding to a thin disc with scale height independent of radius. As ν/κ varies from 2.0 at R_\odot to 1.56 at 25 kpc the ratio σ_Z/σ_R is 0.5 at R_\odot and drops to 0.4 at 25 kpc. The expected vertical density profile $\rho(z)$ is logarithmically sensitive to z/a_{zmax} with a cusp at the midplane. From the initial stellar distribution, we numerically measured the vertical dispersion of the initial density profile at R_\odot finding a width $\sqrt{\langle z^2 \rangle} = 163 \text{ pc}$. We also numerically measured the asymmetric drift $v_a = \langle V_c - V_\theta \rangle \sim 3 \text{ km s}^{-1}$ at R_\odot .

2.2 Perturbations from a Dwarf Galaxy

The orbit of the Sagittarius dwarf galaxy has been inferred from modeling the continuous stream of debris in the Sagittarius dwarf galaxy’s tidal tails (e.g., Johnston et al. 2005; Law & Majewski 2010; Purcell et al. 2011) and resembles a trefoil knot (see Figure 1 by Johnston et al. 2005 and our illustration in Figure 2). The Sagittarius dwarf galaxy nucleus is currently near pericentre in its orbit. The Sagittarius dwarf galaxy nucleus previously passed through the Galactic plane about 0.4 Gyr ago, but at large Galactocentric radius $R \gtrsim 50$ kpc. The previous pericentre occurred about 1 Gyr ago and at positive Z in our Galactocentric coordinate system (see lower left panel of Figure 8 by Law & Majewski 2010). Our illustration in Figure 2 labels the last pericentre as E1. About 2 Gyr ago, the dwarf galaxy’s nucleus passed through the Galactic plane when it was nearly at pericentre. This event is labelled as E2 in our illustration. In Figure 2 we plot a model orbit by Chakrabarti et al. (2014) (that labelled E in their Table 1), that matches the observed proper motions for stars in the Sagittarius dwarf galaxy nucleus. Using this orbit, we list in Table 1 the positions and velocities of the dwarf galaxy nucleus at the E1 pericentre and the E2 passage through the Galactic plane. These two events could have caused large perturbations to the disc stars and we use them to generate velocity perturbations for our test-particle integrations.

After generating a thin disc we use an instantaneous hyperbolic orbit approximation (often used to derive dynamical friction and gravitational heating rates, see Binney & Tremaine 1987 section 7.1) to perturb the velocities of each particle. Two sets of integrations are done, each using a separate encounter listed in Table 1. We use a hyperbolic orbit to compute the velocity perturbations on each particle (applied instantaneously at the beginning of the orbital integration). Our procedure for computing the velocity perturbation from the dwarf encounter positions and velocities in Table 1 is described in more detail in our appendix A. Using this approximation the velocity perturbation $\Delta \mathbf{v}$ is proportional to the mass of the dwarf galaxy, M_d . Hence, perturbations from larger or smaller dwarf galaxy masses can be estimated by scaling the resulting velocity perturbations.

The progenitor dwarf galaxy mass for the E model by Chakrabarti et al. (2014) is $M_d = 10^{10} M_\odot$ and lighter than

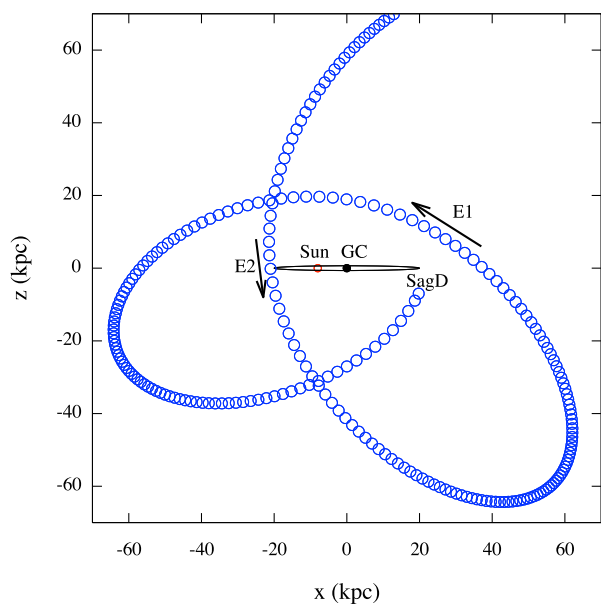


Figure 2. Illustrating the Sagittarius dwarf orbit from the E model by Chakrabarti et al. (2014). The current position of the dwarf in its orbit is labelled “SagD” and the passage through the galactic plane 2.2 Gyr ago labelled with E2 and a black arrow. The previous pericentre, 1.1 Gyr ago, is labelled E1 and shown with another black arrow. Axes are in Galactocentric coordinates and in units of kpc.

both the ‘light’ ($3 \times 10^{10} M_\odot$) and ‘heavy’ ($10^{11} M_\odot$) Sagittarius dwarf galaxy masses explored by Purcell et al. (2011). Purcell et al. (2011); Chakrabarti et al. (2014) take into account dynamical friction and tidal stripping of the dwarf galaxy. The dwarf galaxy mass is similar to its initial mass until pericentre near E2, approximately 2 Gyr ago, at which time the dwarf loses about half of its mass (see Figure S2 by Purcell et al. 2011). The dwarf galaxy mass then remains constant until the E1 pericentre. Consequently, we take the mass of the dwarf to be equal to its progenitor mass for the E2 encounter and half that at the E1 encounter. For the E2 encounter we use a dwarf galaxy mass of $M_{dE2} = 5 \times 10^{10} M_\odot$ (which implies $M_{dE1} = 2.5 \times 10^{10} M_\odot$), in between the light and heavy models by Purcell et al. (2011), but heavier than the E model by Chakrabarti et al. (2014).

2.3 Initial mean velocities

We generate 10 million particles for the E1 and the E2 encounters, separately. Following generation of the thin disc and the instantaneous velocity perturbation due to the E1 or E2 encounters, (and prior to orbit integration) we compute mean velocities in 0.25 kpc square bins in X and Y , summing together the velocity components for all particles within each bin. Figure 3 shows the initial mean radial velocity component, $\langle V_R \rangle$, the mean vertical velocity component $\langle V_Z \rangle$, and the mean tangential velocity component subtracted by the circular velocity as a function of radius, $\langle V_\theta \rangle - V_{circ}(R)$, for the E1 and E2 encounters. The E2 encounter has velocity vector nearly but not exactly perpendicular to the Galaxy

Table 1. Parameters for the two dwarf galaxy encounters labelled in Figure 2

Encounter	t (Gyr ago)	Mass ($\times 10^{10} M_{\odot}$)	\mathbf{v} (km s $^{-1}$)	\mathbf{r} (kpc)
E1	1.1	2.5	(−339, −44, 76)	(4, 8, 18)
E2	2.2	5.0	(4, −111, −337)	(−21, −4, 0)

midplane. The velocity vector is tilted slightly so that the orbit is at positive Z above the midplane at negative Y and vice-versa at positive Y . The tilt of the dwarf’s orbit gives a negative V_Z perturbation to the particles in the disc at positive Y and vice-versa at negative Y . We see this as nearby red and blue regions in the $\langle V_Z \rangle$ panel in Figure 3. These nearby particles differ in vertical epicycle angle, ϕ_z , by π (see equations 2). The situation is different for the E1 encounter. Because the dwarf galaxy passes above the Galactic plane in this encounter, both $\langle V_R \rangle$ and $\langle V_Z \rangle$ are in the same direction, though $\langle V_{\theta} \rangle$ has both positive and negative perturbations (see top panels in Figure 3). Because $\langle V_Z \rangle$ is positive the perturbed particles have the same phase $\phi_z \sim 0$ and the size of $\langle V_Z \rangle$ gives vertical epicyclic amplitude $a_z \sim 0.05$ in units of radius (using a typical V_Z and equations 2). The sign change in the V_{θ} perturbation gives epicyclic angle $\phi_r \sim \pi/2$ where $\langle V_{\theta} \rangle$ is lower than the circular velocity and $\phi_r \sim -\pi/2$ where $\langle V_{\theta} \rangle$ exceeds the circular velocity (using equation 1) and epicyclic amplitude $a_r \sim 0.15$ in units of radius. Even though the dwarf mass used for the E1 encounter is half of that in the E2 encounter, the V_Z perturbation is larger. This is because the E1 encounter has its closest approach above rather than in the Galactic plane. Even though the dwarf mass is lower for the E1 encounter, it is more effective at exciting vertical epicyclic motions.

3 VELOCITY DISTRIBUTIONS AFTER ORBITAL INTEGRATION

Using *galpy*’s Dormand-Prince integrator, the initial particle distributions (with mean velocities shown in Figure 3) are then integrated to the present time (2.2 Gyr for the E2 integration and 1.1 Gyr for the E1 integration). In Figures 4 and 5 we show mean velocities, similar to those presented in Figure 3, as well as the particle density distributions as a function of X, Y for both E1, and E2 encounters, but after orbit integration to the present time. The density distributions shown in Figures 4 and 5 resemble those illustrated by previous works using particle integrations (Quillen et al. 2009) and N-body simulations (Purcell et al. 2011; Gómez et al. 2013; Widrow et al. 2014). We confirm that trailing spiral structure or overdensities can be induced by dwarf galaxy encounters, if the dwarf galaxy mass is similar to $10^{10} M_{\odot}$. Because self-gravity is not present in our simulations, the spiral structure is due to the radial epicyclic motions excited by the encounters that are evident in the initial perturbations to V_R and V_{θ} shown in Figure 3.

In Figures 4 and 5 we also show the mean Z value as a function of X, Y . This is computed in 0.25 kpc square bins in the same way that we compute the mean velocity components. The $\langle Z \rangle$ subpanels in Figures 4 and 5 show that there are large regions of the disc with mean height above or below the galactic midplane, implying that the galaxy disc

has become warped. This phenomenon has also been seen in previous simulations (e.g., see Figure 5 by Gómez et al. 2013). The warp arises as vertical amplitudes induced by the encounter (and seen in the $\langle V_Z \rangle$ distributions just after the encounters in Figure 3) have been sheared due to differential precession and the radial gradient of the vertical epicyclic frequency ν . We note that this warp is not self-consistent as we use a static galactic potential, whereas a warp in the disc would influence the potential. The E1 encounter seen in Figure 4 shows ring – like structure in $\langle Z \rangle$ that is found in similar regions as and resembles the Monoceros and Triangulum – Andromeda overdensities as observed by Xu et al. (2015) and Price-Whelan et al. (2015). We note that the warp for E2 encounter appears to be more twisted than that of the E1 integration. The E2 encounter occurs 2.2 Gyr ago and there are more rotation periods for the phase wrapping to take place.

3.1 Breathing and Bending Coefficients

Breathing and bending modes arise from the self-gravity of the Galactic disc. Breathing modes signify that stars above and below the midplane move in opposing vertical directions, while bending modes imply stars above and below the midplane move en masse upwards or downwards (Sun et al. 2015). To quantify bending and breathing modes Widrow et al. (2014) fit a function to the mean vertical velocity as a function of Z in each X, Y bin,

$$\langle V_Z \rangle(x, y, z) = A_Z(x, y)z + B_Z(x, y) \quad (3)$$

(their equation 24). Here $B_Z(x, y)$ is not equivalent to our computed $\langle V_Z \rangle$ as it is equal to the mean value of V_Z at $Z = 0$, and the density distribution may not be symmetric about $Z = 0$. We use a linear regression to fit for the A_Z coefficient in each 0.25 kpc square bin in X, Y . Widrow et al. (2014) use A_Z to describe breathing modes and B_Z to describe bending modes. The A_Z and B_Z coefficients are also shown in subpanels of Figures 4 and 5. We have measured A_Z and B_Z coefficients with sizes of several km s $^{-1}$ kpc and km s $^{-1}$ respectively for both encounters. Figure 4 shows that the structure of the A_Z and B_Z coefficients in our E1 encounter resembles the spiral structure seen in Figures 10 and 12 in Widrow et al. (2014), though it is necessary to note that these figures from Widrow et al. (2014) occur at different times from our encounters after the initial perturbation. As we have carried out non-interacting test-particle integrations in a fixed potential, these coefficient values and structure cannot be due to bending or breathing waves or modes. Rather, they can only be due to phase wrapping of epicyclic amplitude perturbations.

The perturbing dwarf galaxy is more massive for the E2 encounter, however there is longer time for phase wrapping to occur and the perturbed motions vary in phase. Values for the A_Z coefficient in Figure 5 range from −5 to 5 km s $^{-1}$ kpc

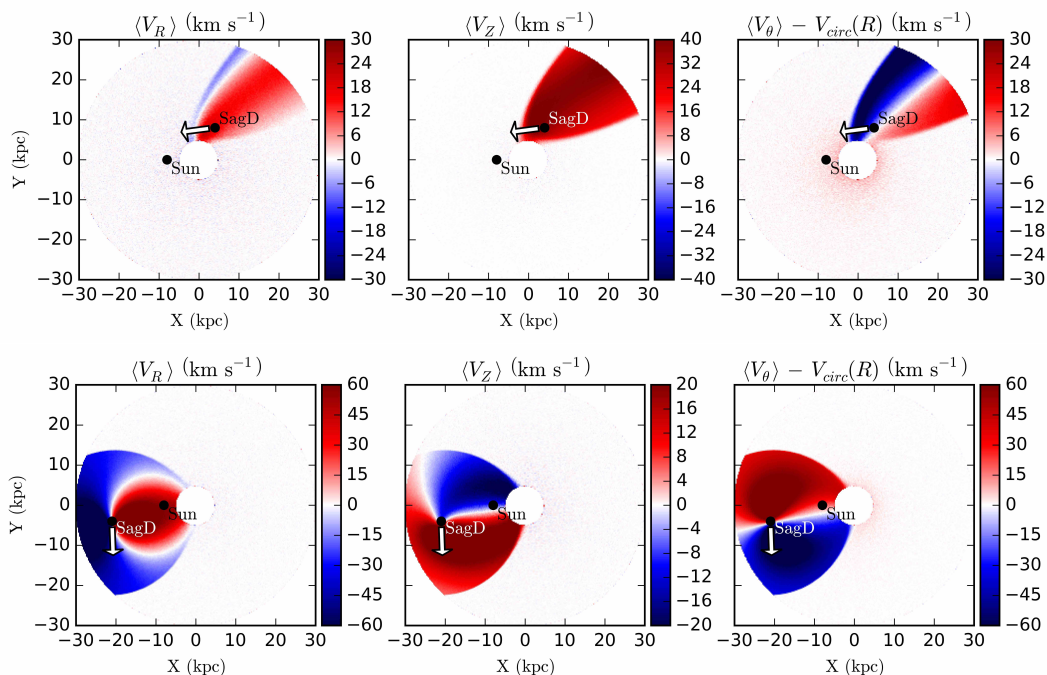


Figure 3. Mean particle velocity distributions as a function of X, Y in the Galaxy prior to orbital integration. The initial thin discs have been instantaneously perturbed using an instantaneous hyperbolic orbit approximation (described in appendix A). In the top panels, we show the mean velocities induced by the pericentre encounter 1 Gyr ago (E1 encounter). The top left panel shows the mean radial velocity component, the top middle panel, the mean vertical velocity component and the top right panel the mean tangential velocity component subtracted by $V_{\text{circ}}(R)$. Each panel displays the position and direction of the Sagittarius Dwarf in X, Y with a black dot and an arrow. For scale the current position of the Sun is also shown, however the Sun would have been at a different azimuthal angle during the encounter. Galactic rotation is counter-clockwise. On the bottom a similar set of panels show mean velocities but for the passage through the Galactic plane 2 Gyr ago (E2 encounter). Parameters for the two encounters are listed in Table 1. Nearby particles differ in vertical epicyclic angles by π for the E2 encounter, whereas they all have the same phase in the E1 encounter. Even though the dwarf mass is lower for the E1 encounter, it is more effective at exciting vertical motions.

but much of the substructure is erased because the structure is so tightly wound. For the E1 simulation, structure in A_Z is more coherent and ranges from -10 to $10 \text{ km s}^{-1} \text{ kpc}$. The extent of variations seen in A_Z in our integrations is nearly the same size as those observed locally; Carlin et al. (2013) and Sun et al. (2015) measure A_Z values in the range -10 to $10 \text{ km s}^{-1} \text{ kpc}$ (see Figure 13 by Sun et al. 2015 and Figure 3 by Carlin et al. 2013). Variations in the value of $\langle V_Z \rangle$ are approximately $\pm 10 \text{ km s}^{-1}$ for both simulations and similar to those observed (see Figure 14 by Williams et al. 2013). While phase wrapping from a relatively massive dwarf galaxy with a single encounter can cause measurable values for the A_Z coefficient, it may not account for the full extent of the observed values.

3.2 The vertical gradient of the mean radial velocity component

To quantify the sensitivity of the radial velocities with height above the Galactic plane we also fit a linear function to the mean radial velocities

$$\langle V_R \rangle(x, y, z) = A_R(x, y)z + B_R(x, y)$$

similar to equation 3 but using V_R and with coefficients A_R, B_R . These maps are computed in the same way as for the A_Z, B_Z coefficients and also shown in Figures 4 and 5.

We can see from these Figures that there are strong correlations between the maps.

3.3 Dynamical Interpretation

Our original velocity perturbations (shown in the initial velocity perturbations in Figure 3) are localised near a particular azimuthal angle (near closest approach) that we can denote Θ_p , however, V_R and V_Z velocity perturbations also extend over a range of radius. We can roughly group stars into two sets: those that are perturbed, and those that remain in circular planar orbits. After 1 or 2 Gyr (depending on the encounter) the dependence of the angular rotation rate on radius, $\Omega(R)$ shears the distribution of perturbed stars. Meanwhile the stars oscillate vertically and radially, at frequencies that depend on their mean radius or angular momentum.

For an initial perturbation at Θ_p , after a time ΔT the perturbation will be wrapped in 2π in azimuthal angle across a radial distance

$$\Delta R \sim \frac{2\pi}{\Omega_{,r}\Delta T} \sim R \frac{P}{\Delta T} \quad (4)$$

where $\Omega_{,r}$ is the radial derivative of the angular rotation rate and $P \sim 0.23 \text{ Gyr}$ is the rotation period at the Sun's Galactocentric radius and we have approximated the rotation curve as a flat one with $V_c(R) = \text{constant}$. For our per-

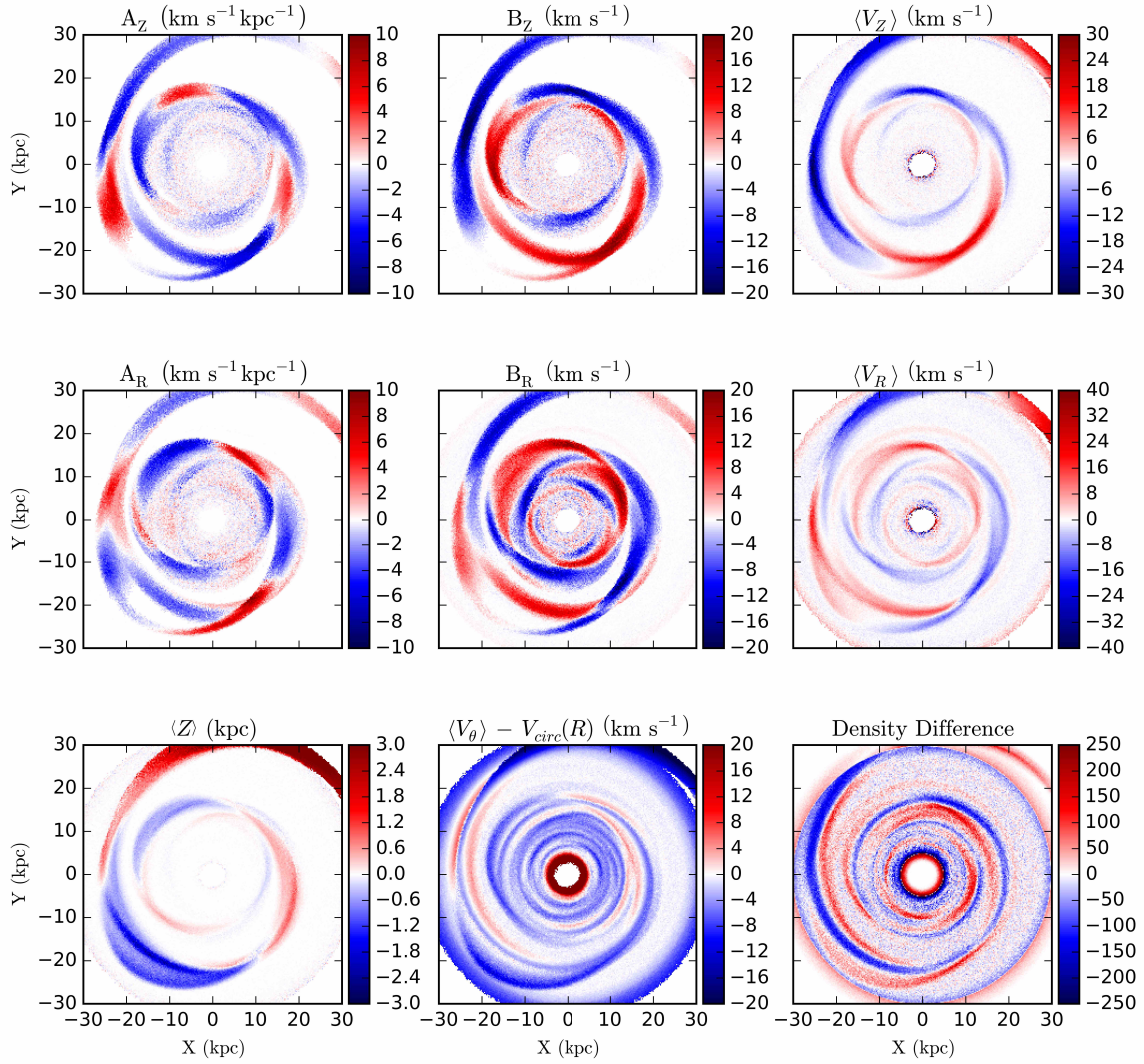


Figure 4. Distribution of mean velocities and A_Z, B_Z, A_R, B_R parameters as a function of X, Y for the E1 encounter after orbit integration to the present time. Top row from left to right, A_Z, B_Z and $\langle V_Z \rangle$, middle row from left to right A_R, B_R and $\langle V_R \rangle$, bottom row, $\langle Z \rangle$, $\langle V_\theta \rangle - V_{\text{circ}}(R)$ and difference between current and initial number densities. Velocities and B_Z, B_R are in km s^{-1} , and the A_Z, A_R coefficients are in $\text{km s}^{-1} \text{ kpc}$. The difference between current and initial densities is shown in numbers of particles per 0.25 kpc square bin.

turbation with $\Delta T = 1$ Gyr ago, $\Delta R \sim 1.8$ kpc. That means that every 1.8 kpc in radius we should encounter stars that were initially in the peak of the perturbed region, however this neglects radial motions in the perturbed stars.

The initial perturbation region, in cylindrical coordinates, is illustrated in Figure 6 in the top left panel as a grey bar. Ignoring the radial motions of the perturbed stars, after a time ΔT later, the distribution of perturbed stars is tilted, as shown in the top panel second from left. Stars outside the perturbed region have little radial motion, so they remain in the region outside the tilted bar but they shear at the same speed. For the E1 encounter, initial $V_z > 0$, giving the perturbed stars an initial epicyclic phase $\phi_z \approx 0$. The grey bar shown in Figure 6 will oscillate vertically as it tilts, after a time ΔT the perturbed stars are at different heights (shown in top panel second from right). Peak to

peak vertical maxima should occur across a radial distance

$$\Delta R_\nu = R \frac{P}{\Delta T} \frac{\Omega}{\nu}. \quad (9)$$

and computing this distance for $\Delta T = 1$ Gyr and $\nu/\Omega \sim 2.6$ (using `galpy`'s Milky Way potential `MWPotential2014`) we estimate $\Delta R_\nu \sim 0.75$ kpc. This we expect is the radial distance between two maxima in Z in the inner region of the galaxy, and it is approximately consistent with what is seen near R_\odot in the lower left panel of Figure 4 showing $\langle Z \rangle$. We compare the peak to peak radial distance from epicyclic phase wrapping to the wavelength predicted for bending waves, $\Delta R_\nu \sim 10$ kpc (Weinberg 1991, see Section 6). The radial distance between peaks in Z can be much smaller than the wavelength predicted for bending waves.

The perturbed stars also oscillate radially. If there is a single phase for ϕ_r for the perturbed stars, then the distribution of the perturbed stars wiggles, as shown by the green

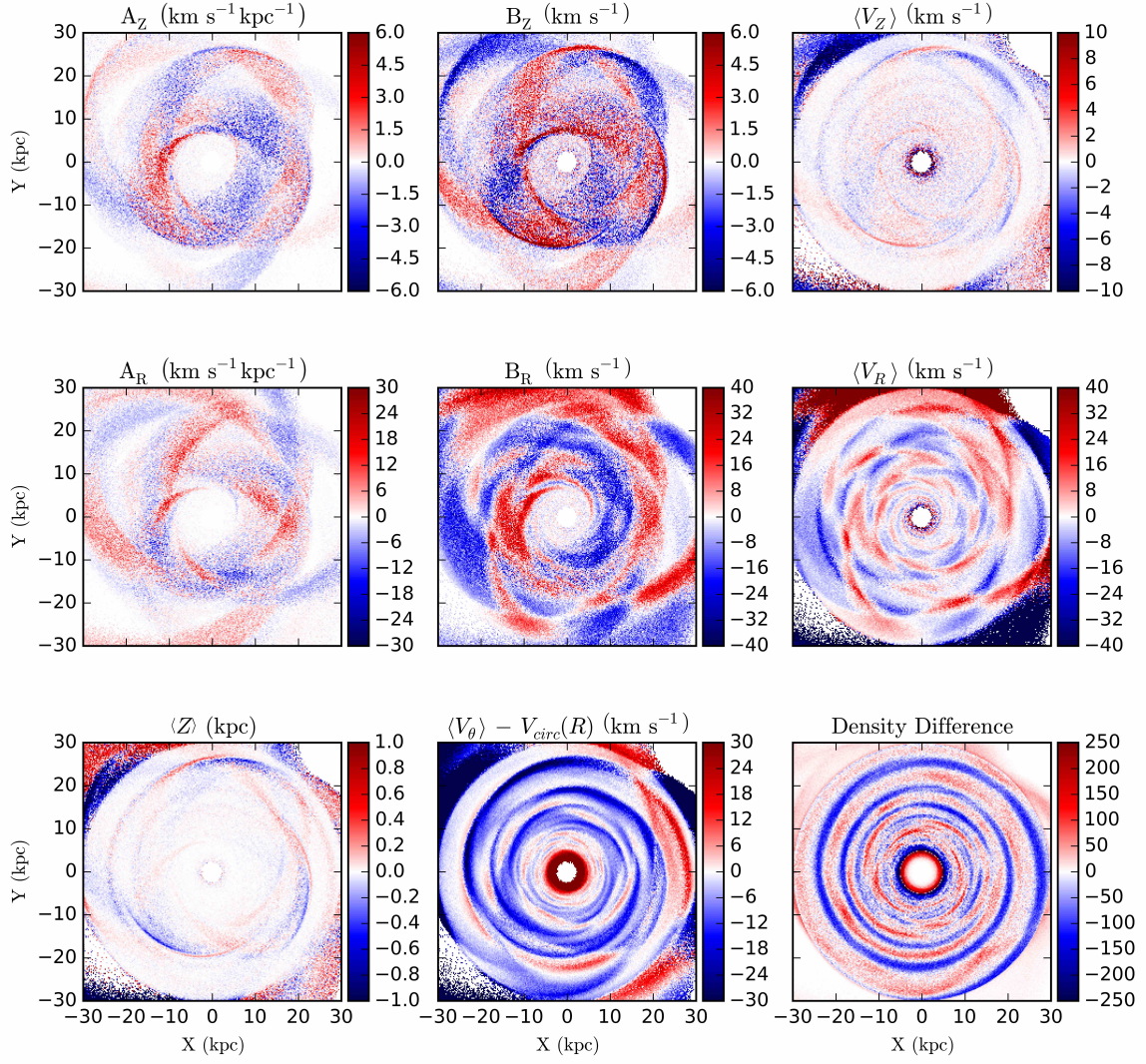


Figure 5. Similar to Figure 4 except for the E2 encounter.

curve on the top right panel. The wiggles in the green curve can lie in the same regions as stars on circular orbits (yellow background). There are overlap regions that would contain higher surface densities of stars accounting for the similar morphology of the density panel and velocity panels in Figure 4. For some R, Θ there are two populations of stars: stars in circular orbits and stars that were perturbed by the encounter. As the stars perturbed by the encounter can reach larger distances above and below the Galactic plane, the combined population can exhibit a vertical velocity gradient. Likewise, there are regions where perturbed stars outnumber unperturbed stars, leading to underdensities that can still exhibit velocity gradients.

The E1 encounter also gives velocity perturbations in V_R and V_θ , resulting in a region of the galaxy with stars that all have an epicyclic angle $\phi_r \sim -\pi/2$ for Θ slightly lower than the center Θ_p and $\phi_r \sim \pi/2$ for Θ slightly higher than the center, the change in sign resulting from the azimuthal variation in V_θ (see Figure 3). We can consider a localised (in Θ) increase in epicyclic amplitudes a_r and a_z , with $\phi_z = 0$, near the center and $\phi_r = -\pi/2$ but flipping sign at Θ_p . This

situation is represented in the lower left panel in Figure 6 and after shearing in Θ in the lower panel, second from left. Vertical oscillations are in phase and shown in the lower panel second from right. Because the epicyclic frequency, (κ) and vertical oscillation frequency (ν) depend on radius as the region of perturbation is stretched, it also oscillates radially and up and down. A perturbation in the radial direction and initially all in phase in ϕ_r will be wrapped in its radial epicyclic by 2π (corresponding to two particles each at pericentre) across a radial distance

$$\Delta R_\kappa = R \frac{P}{\Delta T} \frac{\Omega}{\kappa} \quad (6)$$

Using $\kappa/\Omega \sim 1.4$ we estimate $\Delta R_\kappa \sim 1.3$ kpc near the Sun. If all perturbed particles were initially in phase then we would expect the distance between radial oscillation maxima to be 1.3 kpc, however the ϕ_r varies by almost π in the initial perturbation and this gives about twice as many oscillations. Furthermore, perturbed stars can overlay each other as well as overlay unperturbed stars (as shown in bottom right panel in Figure 6). The two effects likely account for the increased

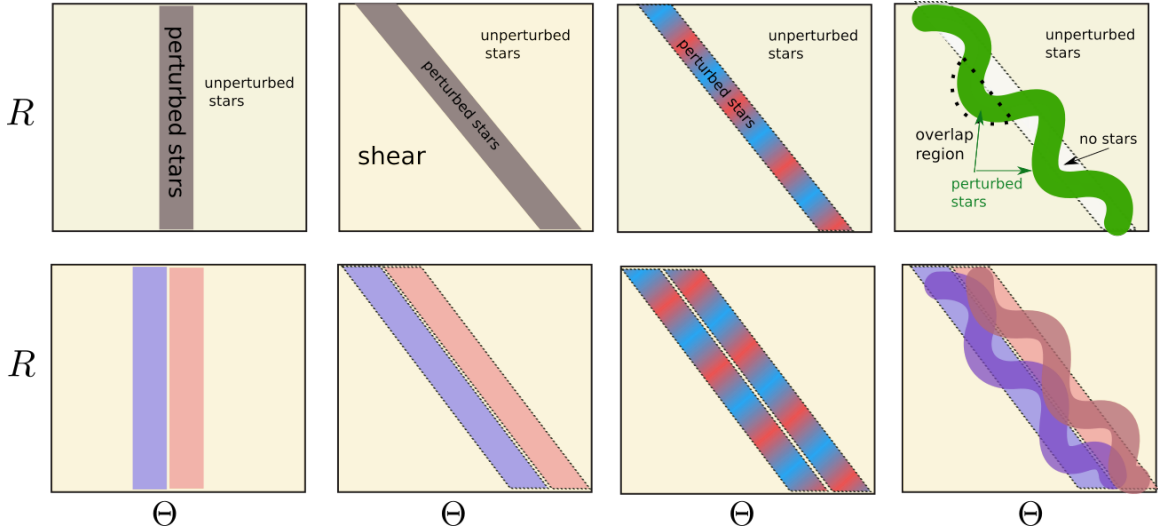


Figure 6. A perturbation localised in Θ but extending in R is shown on the top left panel. After a time ΔT the perturbation shears due to differential rotation (top panel second from left). Taking into account the frequency of vertical oscillations, the perturbed stars move up and down (top panel second from right). Taking into account a perturbation in radial epicyclic and assuming the perturbation has a single phase in radial epicyclic angle ϕ_r , the radial motions deform the distribution of perturbed stars giving the green curve on the top right panel. Where the green curve lies outside the white bar, perturbed stars are found at the same R, Θ as unperturbed stars and the combined populations can give vertical gradients in the velocity components. The E1 encounter initially has both positive and negative changes to V_θ giving epicyclic phases that are both positive and negative (shown on the bottom left panel) and after shearing due to differential rotation (shown in the bottom panel second from left). Vertical oscillations are in phase and shown in bottom panel second from right. The radial excursions from each bar have opposite sign and so can overlap one another as well as unperturbed stars (shown on bottom right panel).

number of red and blue regions in the A_R and B_R panels compared to the A_Z and B_Z panels shown in Figure 4.

In Figure 4 the $\langle V_Z \rangle$ and $\langle Z \rangle$ subpanels resemble each other except they are 90° out of phase, as would be expected from vertical oscillations of the perturbed stars. The A_Z slope coefficient measures the gradient of $\langle V_Z \rangle$ with Z . In regions where stars in the midplane coexist with (or overlap) perturbed stars, a gradient is measured when the perturbed stars lie above or below the Galactic plane and there are unperturbed stars in the midplane. Where the perturbed particles are above the plane ($Z > 0$) but moving downward ($V_Z < 0$), we estimate the gradient from these stars and the unperturbed ones in the midplane with $V_Z \sim 0$, giving approximately $A_Z \sim \langle V_Z \rangle / \langle Z \rangle$ and A_Z is negative. For stars below the plane ($Z < 0$) with $V_Z < 0$, $A_Z > 0$. Thus, we expect the A_Z map contains twice as many color features as the $\langle Z \rangle$ and $\langle V_Z \rangle$ maps and indeed that is what we see on the top left in the A_Z panel of Figure 4, when compared to the $\langle V_Z \rangle$ and $\langle Z \rangle$ panels.

Similar phenomena are seen in Figure 5, showing the E2 encounter, except there are many more features in each panel. This is expected as the time to wrap in phase is twice as long, but in addition the initial perturbation contains regions differing in phase ϕ_z and ϕ_r also contains additional structure as initial V_R and V_Z distributions are more complex than for the E1 encounter (see Figure 3). Because the E2 encounter is less effective at inducing vertical oscillations and much of induced structure is erased due to the long timescale and higher complexity of the epicyclic phases, hereafter we primarily discuss the E1 encounter.

Noticeable correlations between the density of stars and different velocity components exist in our simulations. Fig-

ures 4 and 5 show that regions that have extreme velocity means are the same as regions with extreme gradients, and these are the same as those with high or low surface densities. Perturbed stars lie chiefly in regions where the mean velocity component is nonzero and there are overdensities or underdensities. As perturbed stars lack circular orbits, they have radial velocity components that affect their tangential velocities; in general, positive $\langle V_R \rangle$ gives negative $\langle V_\theta \rangle - V_{\text{circ}}(R)$, and this occurs where there are overdensities in our integrations. Differences in bulk radial velocities can result in separated overdensity streams, where bands of stars share the same density but have split off from each other, such as those seen around $(X, Y) = (-15, 15)$ kpc and $(X, Y) = (5, 10)$ kpc in the density panel in Figure 4. These disparities in $\langle V_R \rangle$ also produce bifurcations, or ‘forked - tongue’ patterns, in $\langle V_Z \rangle$, seen in the upper right panel in Figure 4.

Negative values of $\langle V_\theta \rangle - V_{\text{circ}}(R)$ (corresponding to positive asymmetric drift) are expected from a steady state disk, though here the density, mean velocity components and dispersions are time dependent. Because the initial density distribution is proportional to $1/R$ we expect that eccentric particles are more likely to affect the velocity mean near apocenter where V_θ is lower than that of particles in circular orbits, rather than near pericenter where V_θ is higher than that of particles in circular orbits.

Vertical velocity gradients are seen in our numerical integrations and they can be explained by vertical and radial epicycle motions excited by the encounters. The vertical gradients arise in regions where perturbed and unperturbed stars (or different source regions of perturbed populations) lie in the same X, Y region. Because they arise due to overlap

of different populations we expect (and see in our integrations) strong correlations between the distributions of the different velocity components and the density. The number of peaks in $\langle Z \rangle$ or $\langle V_Z \rangle$ can roughly be estimated using a shearing timescale based on the oscillation frequency and the timescale since the perturbing encounter.

3.4 Local Velocity Gradients

To mimic observations of nearby stars in the Galaxy we can extract test particles in small regions of the Galaxy. Sun et al. (2015) (in their Figures 13 and 14) showed linear fits to $\langle V_Z \rangle$ with Z at different locations in X, Y near the Sun. We construct here a similar figure to illustrate that our integrations display gradients in the vertical velocity component. A matrix containing numbers of particles is constructed in ($8 \leq R \leq 10$ kpc, $176^\circ \leq \Theta \leq 184^\circ$, $-1 \leq Z \leq 1$ kpc) with binning size $(\Delta R, \Delta \Theta, \Delta Z) = (0.25 \text{ kpc}, 2^\circ, 0.25 \text{ kpc})$. After generating the number density matrix, we apply the same outlier rejection criteria used by Sun et al. (2015), namely requiring $-200 < V_R < 200 \text{ km s}^{-1}$, $0 < V_\theta < 400 \text{ km s}^{-1}$ and $-200 < V_Z < 200 \text{ km s}^{-1}$ to compute a velocity matrix in $\langle V_Z \rangle$; we then divide the velocity matrix by the number density matrix to yield a bulk or mean V_Z matrix in R, Θ and Z . We use linear regression to find the best fit line of

$$\langle V_Z \rangle(R, \theta, z) = A_Z(R, \theta)z + B_Z(R, \theta)$$

for each pair of (R, Θ) . The individual values for $\langle V_Z \rangle(z)$ are shown in Figure 7 at $\Theta = 180^\circ$ along with the linear fits giving us A_Z and B_Z coefficients; the X, Y axes of each sub-panel correspond to $-2 \leq Z \leq 2$ kpc and $-30 \leq \langle V_Z \rangle \leq 30 \text{ km s}^{-1}$, respectively. In the previous section we attributed the velocity gradients to overlap of populations of perturbed and unperturbed stars. However, most of the panels in Figure 7 show smooth variations in mean velocities as a function of height above and below the Galactic midplane. Had we started with a planar thin disc in circular orbits we would have seen folds in the disc and these would not have given smooth velocity gradients. We can attribute the smooth slopes to the velocity dispersion in our initial disc. Sun et al. (2015) (and others) measured different velocity gradients in different regions of the galaxy. Figure 7 shows that there are rapid variations in velocity gradients with position in our simulated Galaxy. Hence some or all of the fine structure measured by Sun et al. (2015) and Carlin et al. (2013) might be real, and we might expect that future observations extending the number of stars, precision and distance of stars will uncover even more structure in the velocity field.

We now explore whether our integration can exhibit the patterns seen as a function of Z in recent observational studies. A key feature seen in the local velocity distributions is a strong vertical gradient in $\langle V_Z \rangle$ with negative V_Z at positive Z and a slope of $A_Z \sim -5$ to $-10 \text{ km s}^{-1} \text{ kpc}$ (Carlin et al. 2013; Williams et al. 2013). Regretfully, in Figure 4 $A_Z > 0$ at $(-R_\odot, 0, 0)$ and so is not consistent with the observed pattern of gradients near the Sun. As the gradients are comprised of tightly wound structures, they are sensitive to the time since the encounter. We can effectively vary the time since encounter by considering different angular locations in the Galaxy at the same radius as the

Sun. The rotation period at the Sun is $P \sim 0.23$ Gyr, hence an uncertainty in the time since the E1 encounter of only 0.1 Gyr would give rotation by nearly 180° . Estimates of the time since the last pericentre encounter range from 0.8 to 1.1 Gyr. For example, Purcell et al. (2011) give a time and distance for last pericentre for the Sagittarius dwarf galaxy of $t_{\text{peri}} \approx 0.85$ Gyr ago, $R_{\text{peri}} \approx 15$ kpc for their light model and $t_{\text{peri}} \approx 1.1$ Gyr ago, $R_{\text{peri}} \approx 15$ kpc for their heavy model. Law & Majewski (2010) in their Figure 7 give $t_{\text{peri}} \approx 0.8$ Gyr ago, $R_{\text{peri}} \approx 15$ kpc for the Sagittarius dwarf.

In Figures 8, we emulate Figures 10, 12 and 13 by Williams et al. (2013) and Figure 2 by Carlin et al. (2013) by plotting gradients of $\langle V_R \rangle$, $\langle V_\theta \rangle - V_\odot$, and $\langle V_Z \rangle$ in different local neighbourhoods for encounter E1 in (R, Z) with $6 \leq R \leq 10$, $-2 \leq Z \leq 2$ kpc and Θ in 45° increments with a 16° spread using bin sizes of $(\Delta R, \Delta Z) = (0.25, 0.25)$ kpc. We generate mean velocity matrices in the same method as previously above. The resulting mean velocities are smoothed with a Gaussian filter with $\sigma_Y, \sigma_X = 1$ to reduce the graininess resulting from the particle distributions. Like Figures 4 and 5 we only show in Figure 8 the distribution at a particular time since encounter, but the structure would be different if the encounter occurred earlier or later. Figure 8 shows that there is potentially quite a bit of structure in the bulk velocities above and below the Galactic plane, and that there could be large variations in the vertical gradients as a function of R, Θ as well as Z . If phase wrapping of epicyclic perturbations is responsible for the observed variations in bulk velocities, a consequence would be predicted variations in the bulk velocity as a function of distance from the Sun, such as the symmetry in $\langle V_R \rangle$ and $\langle V_\theta \rangle - V_\odot$ above and below the midplane.

Figure 8 illustrates that there are regions in our simulated galaxy that show negative vertical velocity gradients in $\langle V_Z \rangle$. For example, the second panel corresponding to $\Theta = 45^\circ$, displays negative V_Z above the Galactic plane for $R > 8$ kpc and vice versa below the Galactic plane, giving A_Z with the expected and observed sign and about the right size. The velocities near the midplane in most regions are approximately zero, consistent with the presence of unperturbed stars in the extracted neighbourhoods. The largest velocities are seen away from the Galactic plane, consistent with the presence of perturbed stars. However, as we did not include a thick disc component in our initial particle distributions, above and below the Galactic plane are found only perturbed particles and these dominate the mean velocities. Had we included a thick disc component we could have measured lower gradients as they could have diluted the contribution from the perturbed stars. We adopted a $1/R$ number density to increase the number of particles at large radius, and this too would bias our computed values of A_Z and B_Z .

Carlin et al. (2013) show negative $\langle V_R \rangle \sim -5 \text{ km s}^{-1}$ near the midplane and positive $\langle V_R \rangle \sim 5 \text{ km s}^{-1}$ above and below the midplane. Our integrations primarily show a zero value of $\langle V_R \rangle$ in the midplane because unperturbed disc particles are in nearly circular motion. However, in many of the rows shown in Figure 8 the $\langle V_R \rangle$ distributions are symmetrical at positive and negative Z , such as in the plot at 45° . We attribute this to the fact that $\nu \sim 2\kappa$ throughout the disc, so vertical epicyclic motions have sheared out more

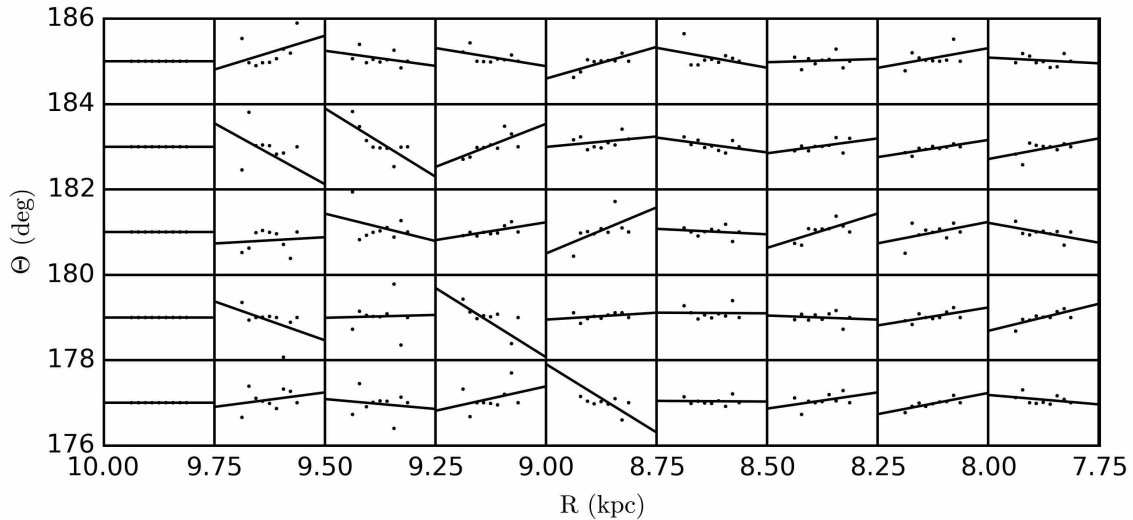


Figure 7. Mock observations of the solar neighbourhood for breathing and bending mode parameters A_Z and B_Z similar to [Sun et al. \(2015\)](#) Figures 13 and 14 for encounter E1. Each subpanel is at a different central Θ and R with values for Θ and R shown on the left and bottom. The X axis of each subpanel has range $-2 \leq Z \leq 2$ kpc and the Y axis $-30 \leq \langle V_Z \rangle \leq 30$ km s $^{-1}$, the linear fits showing vertical gradients in V_Z . This local neighbourhood shows smooth variations in mean velocity components as a function of Z . The gradients in the mean velocities vary rapidly with position in the simulated disc.

than have radial epicyclic motions, leaving the radial structure more coherent. This symmetry is exhibited in numerous extracted regions in Figure 8, though the 45° panel shifts between negative and positive V_R at about $R = 8$ kpc. [Carlin et al. \(2013\)](#) shows a negative value for V_R at $|Z| < 300$ pc so the velocities could be associated with self-gravitating spiral density waves, and these are not present in our integrations. One last thing to point out is that the $\langle V_\theta \rangle - V_\odot$ panels show regions that are both positive and negative above and below the plane (usually symmetrical above and below the plane). Asymmetric drift associated with a thick disc high velocity dispersion would lower the tangential velocity component. If perturbed populations of stars dominate at high and low galactic latitude, one would have to take care not to misinterpret the mean tangential velocity components.

In summary, mock observations of our simulation at R_\odot and different azimuths show that perturbing the disc with a fairly massive Sagittarius dwarf yields measurable gradients with similar sizes compared to recent observations. The vertical velocity component varies smoothly with Z and has slope that varies quickly with position in the Galaxy (Figure 7), mimicking measurements by [Sun et al. \(2015\)](#). Mean velocities as a function of $\langle Z \rangle$ (Figure 8) display gradients and symmetry above and below the midplane similar to those found by [Carlin et al. \(2013\)](#); [Williams et al. \(2013\)](#), however we do not identify a particular region in our simulated galaxy that matches the gradients of all observed velocity components.

4 SUMMARY AND CONCLUSION

Non-interacting test particle integrations in a fixed potential are less accurate than N-body simulations. However, they have the advantage that the role of phase-wrapping of epicyclic perturbations can be studied in isolation from

phenomena that require self-gravity such as bending and breathing waves and modes. We start with a thin disc containing stars subjected to a velocity impulse computed from an instantaneous hyperbolic orbit approximation from a single close encounter with a dwarf galaxy. Particles are then integrated forward to the present time in a fixed Galactic potential and during this time the distribution of epicyclic angles is progressively sheared due to the dependence of vertical and radial epicyclic oscillation frequencies on mean orbital radius. To illustrate this process we use two encounters taken from estimated orbits for the Sagittarius dwarf galaxy nucleus. After the orbit integration the mean velocities of the stars display vertical velocity gradients that have been previously interpreted in terms of breathing and bending modes or waves. However, because our integrations lack self-gravity, these phenomena must instead be due to shearing or phase wrapping of epicyclic perturbations caused by the encounters.

Because the encounter excites radial perturbations, the perturbed particle distribution not only shears with azimuthal angle but wiggles, overlapping the distribution of unperturbed particles. We attribute the measured vertical gradients in bulk velocities to regions where perturbed and unperturbed particles overlap or are found at the same projected X, Y in Galactocentric coordinates, or regions where primarily perturbed stars are located, where underdensities would occur. A vertical gradient arises when a population of perturbed stars lies above or below the plane and its velocity components are compared to those of unperturbed particles that lie in the midplane. Vertical gradients could also arise when different populations of perturbed stars overlaid the same X, Y location. This scenario predicts correlations between vertical gradients of different velocity components and density. The number of peaks in radial or vertical velocity means can be estimated from the time since the en-

counter and the phases in epicyclic angles induced by the encounter.

This work solely considers epicyclic phase wrapping on the Galaxy after an encounter from an external perturber. Effects from internal perturbations, such as spiral arms or a bar, or those due to self-gravity, such as breathing and bending modes, are not present in our integrations. Because phase wrapping of epicyclic perturbations can produce vertical gradients in bulk velocities, breathing and bending modes are not required to account for these gradients. The wavelength of bending waves near the Sun has been estimated to be quite large (~ 10 kpc [Weinberg 1991](#)) implying that variations in bulk velocities over short distances must be due to coherent epicyclic motions, rather than self-gravitating waves or modes. That is not to say that self-gravity has no effect. Internal structures such as spiral density waves or the Galactic bar might also induce velocity gradients ([Faure et al. 2014](#); [Monari et al. 2015](#)). An external perturber in the outer disc would produce gradients in bulk velocities that increase in magnitude with increasing distance from the centre of the galaxy, while an internal perturber (such as the bar) would exhibit gradients with decreasing magnitude with larger radius (e.g., [Monari et al. 2015](#)), so future observations could differentiate between the two mechanisms. The radial distance in maxima of $\langle Z \rangle$, compared to bending wavelengths, may make it possible to distinguish bending waves from epicyclic phenomena. Unfortunately, studies of breathing modes have been restricted to the plane parallel setting ([Widrow et al. 2014](#); [Widrow & Bonner 2015](#)) and so do not predict structure as a function of position in the Galaxy.

We find that the simulated sizes of the A_Z and B_Z coefficients, used to quantify gradients of bulk vertical motions by [Widrow et al. \(2014\)](#), are similar to those observed by [Sun et al. \(2015\)](#) for a moderate mass Sagittarius dwarf galaxy, $\sim 2.5 \times 10^{10} M_\odot$, that passed its orbital pericentre about a Gyr ago. The passage of the Sagittarius galaxy through the Galactic plane approximately 2 Gyr ago is less effective than the pericentre at approximately 1 Gyr ago for three reasons. The extent of phase wrapping is more extreme and warping more tightly wound. Secondly, the E2 perturbation itself excites vertical epicyclic motions that vary in phase by π , whereas the pericentre encounter 1 Gyr ago, because it passes above the disc, excites vertical epicyclic motions in phase. Thirdly, even though we used a larger mass for the E2 encounter, the size of vertical velocity perturbations is smaller than that for the E1 encounter because of the orientation of the encounter.

Regions at a solar neighbourhood radius extracted from our E1 integrations can show negative values of the A_Z coefficient, similar to that recently measured in the Solar neighbourhood ([Carlin et al. 2013](#); [Williams et al. 2013](#)) but not at our expected location of the Sun in the simulation. However, a small error in the time estimated since the latest encounter could account for this discrepancy. We fail to find a local region in the E1 integration that matches the observed vertical gradients of all velocity components. Our integrations do illustrate that phase wrapping of epicyclic perturbations caused by the Sagittarius dwarf galaxy might account for much of structure seen in bulk velocity motions away from the Galactic plane, and if so, there should be large variations in the bulk motions with position in the Galaxy.

We simulate two perturbations from the Sagittarius dwarf galaxy, each with different mass at different times and positions, from one orbit of the dwarf galaxy. If the dwarf is massive enough that dynamical friction is important, then the initial mass of the Sagittarius dwarf affects the orbit ([Purcell et al. 2011](#)), further contributing to the uncertainties in orbital parameters for our encounters. It is possible that the Galactic disc could have been more recently perturbed by an as yet unidentified dwarf, as proposed by [Chakrabarti & Blitz \(2009\)](#).

In this paper we have used highly simplified integrations to isolate epicyclic phase wrapping from other phenomena. The impulse approximation for the encounters could overestimate the energy transfer to the Galactic disc ([D’Onghia et al. 2010](#)), as disc response and time dependence of encounters have not been taken into account. Our orbit integration neglects spiral structure and associated radial migration that would vary oscillation frequencies and so cause a loss of coherence in the epicyclic phases (e.g., [Vera-Ciro & D’Onghia 2015](#)). Self-gravity would also cause variations in the epicyclic amplitudes and angles and so might need to be taken into account to relate structure in the velocity field to a previous encounter. A future comparison between simulations with gravitationally interacting particles and non-interacting particles could be used to identify and study possible bending waves or breathing modes that might be present in N-body simulations. Test particle simulations could be used to improve understanding of the role of the time dependence of the encounters and relate the size scale and distribution of velocity gradients and bulk motions to the perturbations themselves. Thus, improved numerical models and observations might together match the observed gradients and simultaneously better constrain the mass and orbit of the Sagittarius dwarf galaxy.

ACKNOWLEDGEMENTS

We thank Ivan Minchev for valuable comments and the University of Wisconsin, Madison for hospitality in spring 2015. This work acknowledges support from REU program NSF grant NSF-PHY 1460352 and was in part supported by NASA grant NNX13AI27G. ED gratefully acknowledges the support of the Alfred P. Sloan Foundation and the hospitality of the Aspen Center for Physics, funded by NSF Grant No. PHY-1066293. This work is partially funded by NSF Grant No. AST-1211258 and ATP-NASA Grant No. NNX14AP53G.

REFERENCES

- Binney, J., & Tremaine, S. 1987, *Galactic Dynamics*, Princeton University Press, Princeton, NJ
- Bovy, J. 2015, *ApJS*, 216, 29 `galpy`: A python Library for Galactic Dynamics
- Carlin, J. L., DeLaunay, J., Newberg, H. J., et al., 2013, *ApJL*, 777, L5 Substructure in Bulk Velocities of Milky Way disc Stars
- Chakrabarti, S. & Blitz, L. 2009, *MNRAS*, 399, L118 Tidal imprints of a dark subhalo on the outskirts of the Milky Way
- Chakrabarti, S., Quillen, A., Chang, P., & Merritt, D. 2014 Estimating Progenitor Masses of Tidally Disrupting Satellites

using an eccentricity mass relation <http://arxiv.org/abs/1401.4182>

Cincotta, P. M., Muzzio, J. C., Nunez, J. A. 1991, CeMDA, 52, 263 Analytical derivation of the probability for the escape of stars from colliding galaxies

Cui, X.-Q., Zhao, Y.-H., Chu, Y.-Q., et al. 2012, Research in Astronomy and Astrophysics, 12, 1197

D’Onghia, E., Vogelsberger, M., Faucher-Giguere, C., & Hernquist, L. 2010, ApJ, 725, 353 Quasi-resonant Theory of Tidal Interactions

Gauthier, J.-R., Dubinski, J., Widrow, L. M. 2006, ApJ, 653, 1180 Substructure around M31: Evolution and Effects

Gómez, F. A., Minchev, I., O’Shea, B. W., Beers, T. C.; Bullock, J. S., Purcell, C. W. 2013, MNRAS, 429, 159 Vertical density waves in the Milky Way disc induced by the Sagittarius dwarf galaxy

Faure, C., Siebert, A. & Famaey, B. 2014, MNRAS, 440, 2565–2575 Radial and vertical flows induced by galactic spiral arms: likely contributors to our wobbly Galaxy?

Hernquist, L. 1990, ApJ, 356, 359 An analytical model for spherical galaxies and bulges

Johnston, K. V., Law, D. R., Majewski, S. R. 2005, ApJ, 619, 800 A Two Micron All Sky Survey View of the Sagittarius Dwarf Galaxy. III. Constraints on the Flattening of the Galactic Halo

Kazantzidis, S., Bullock, J. S., Zentner, A. R., Kravtsov, A. V., & Moustakas, L. A. 2008, ApJ, 688, 254 Cold Dark Matter Substructure and Galactic discs. I. Morphological Signatures of Hierarchical Satellite Accretion

Law, D. R., Majewski, S. R. 2010, ApJ, 714, 229 The Sagittarius Dwarf Galaxy: A Model for Evolution in a Triaxial Milky Way Halo

Maccio, A. V., Dutton, A. A., van den Bosch, F. C. 2008, MNRAS, 391, 1940 Concentration, spin and shape of dark matter haloes as a function of the cosmological model: WMAP1, WMAP3 and WMAP5 results

Minchev, I., Quillen, A. C., Williams, M., Freeman, K. C., Nordhaus, J., Siebert, A., Bienaymé, O. 2009, MNRAS, 396, 56 Is the Milky Way ringing? The hunt for high-velocity streams

Monari, G., Famaey, B., & Siebert, A. 2015, <http://arxiv.org/abs/1505.07456> The vertical effects of disc non-axisymmetries from perturbation theory: the case of the Galactic bar

Newberg, H. J., Yanny, B., Rockosi, C., et al. 2002, ApJ, 569, 245

Nordström, B., Mayor, M., Andersen, J., Holmberg, J., Pont, F., Jørgensen, B. R., Olsen, E. H., Udry, S., Mowlavi, N. 2004, A & A, 418, 989 The Geneva-Copenhagen survey of the Solar neighbourhood. Ages, metallicities, and kinematic properties of ~14 000 F and G dwarfs

Price-Whelan, A. M., Johnston, K. V., Sheffield, A. A., Laporte, C. F. P. & Sesar, B. 2015, MNRAS 452, 676 A reinterpretation of the Triangulum-Andromeda stellar clouds: a population of halo stars kicked out of the Galactic disc

Purcell, C. W., Bullock, J. S., Tollerud, E. J., Rocha, M., & Chakrabarti, S. 2011, Nature, Vol. 477, No. 7364, pp. 301–303 The Sagittarius impact as an architect of spirality and outer rings in the Milky Way

Quillen, A. C., Minchev, I., Bland-Hawthorn, J., Haywood, M. 2009, MNRAS, 397, 1599 Radial mixing in the outer Milky Way disc caused by an orbiting satellite

Siebert, A., Famaey, B., Minchev, I., Seabroke, G. M., et al. 2011, MNRAS, 412, 2026 Detection of a radial velocity gradient in the extended local disc with RAVE

Spitzer, L. 1958 ApJ, 127, 17

Steinmetz, M., Zwitter, T., Siebert, A., et al. 2006, AJ, 132, 1645

Sun, N.-C. Liu, X.-W., Huang, Y., Yuan, H.-B., Xiang, M.-S., Zhang, H.-W., Chen, B.-Q., Ren, J.-J., Wang, C., Zhang, Y., Hou, Y.-H., Wang, Y.-F., & Yang, M. 2015, in press Galactic disc Bulk Motions as Revealed by the LSS-GAC DR2 <http://arxiv.org/abs/1505.08060v1>

Xu, Y., Newberg, H. J., Carlin, J. L., Liu, C., Deng, L., Li, J., Schonrich, R., & Yanny, B. 2015, ApJ, 801, 105 Rings and Radial Waves in the disc of the Milky Way

Vera-Ciro, C., & D’Onghia, E. 2015, ApJ, submitted, On the conservation of the vertical action on galactic disks <http://arxiv.org/abs/1508.05965>

Weinberg M. D., 1991, ApJ, 373, 391 Vertical oscillation of the Galactic disc

Widrow, L. M., Gardner, S., Yanny, B., Dodelson, S., & Chen, H.-Y. 2012, ApJL, 750, L41 Galactoseismology: Discovery of Vertical Waves in the Galactic disc

Widrow, L. M., Barber, J., Chequers, M. H., & Cheng, E. 2014, MNRAS, 440, 1971–1981 Bending and breathing modes of the Galactic disc

Widrow, L. M., & Bonner, G. 2015, MNRAS 450, 266 Vertical oscillations of fluid and stellar discs

Williams, M. E. K., Steinmetz, M., Binney, J., et al. 2013, MNRAS, 436, 101 The wobbly Galaxy: kinematics north and south with RAVE red clump giants

Younger, J. D., Besla, G., Cox, T. J., et al. 2008, ApJ, 676, L21 On the Origin of Dynamically Cold Rings around the Milky Way

APPENDIX A: INSTANTANEOUS HYPERBOLIC ORBIT APPROXIMATION FOR VELOCITY PERTURBATIONS

We approximate the perturbation caused by the passage of the dwarf galaxy through the Galaxy midplane (E2 encounter) and pericentre encounter (E1 encounter) with a velocity impulse. Each star’s velocity is changed instantaneously. The velocity perturbation is estimated assuming that the encounter can be approximated with a hyperbolic orbit (e.g., see (Binney & Tremaine 1987 section 7.1). We use an instantaneous hyperbolic orbit approximation rather than the impulse approximation (Spitzer 1958) (the high velocity limit of the hyperbolic orbit approximation) because the E2 encounter velocity is oriented nearly perpendicular to the disc. When the perturber velocity vector is perpendicular to the disc, the impulse approximation gives no vertical velocity perturbation to stars in the disc, making it impossible to explore the role of vertical epicycle phase wrapping. However, the more accurate hyperbolic orbit approximation gives a small velocity perturbation in the direction opposite to the velocity vector and so there is a vertical velocity perturbation.

A low mass particle encountering mass M with a relative velocity \mathbf{V} and with impact parameter b on a hyperbolic orbit has, after the encounter, a change in velocity

$$\Delta v_{\perp} = \frac{2bV^3}{GM} \left(1 + \frac{b^2V^4}{G^2M^2} \right)^{-1} \quad (\text{A1})$$

$$\Delta v_{\parallel} = 2V \left(1 + \frac{b^2V^4}{G^2M^2} \right)^{-1} \quad (\text{A2})$$

(Binney & Tremaine 1987 section 7.1) where Δv_{\perp} is in the direction toward position of closest approach and Δv_{\parallel} is in the opposite direction of the relative velocity vector of M and the low mass particle.

To compute the impact parameter and vertical and parallel direction vectors we consider linear trajectories for both star and dwarf galaxy, $\mathbf{x}_d(t) = \mathbf{x}_{d0} + \mathbf{v}_d(t - t_0)$ for the dwarf galaxy with position and velocity \mathbf{x}_{d0} and \mathbf{v}_d at time t_0 when

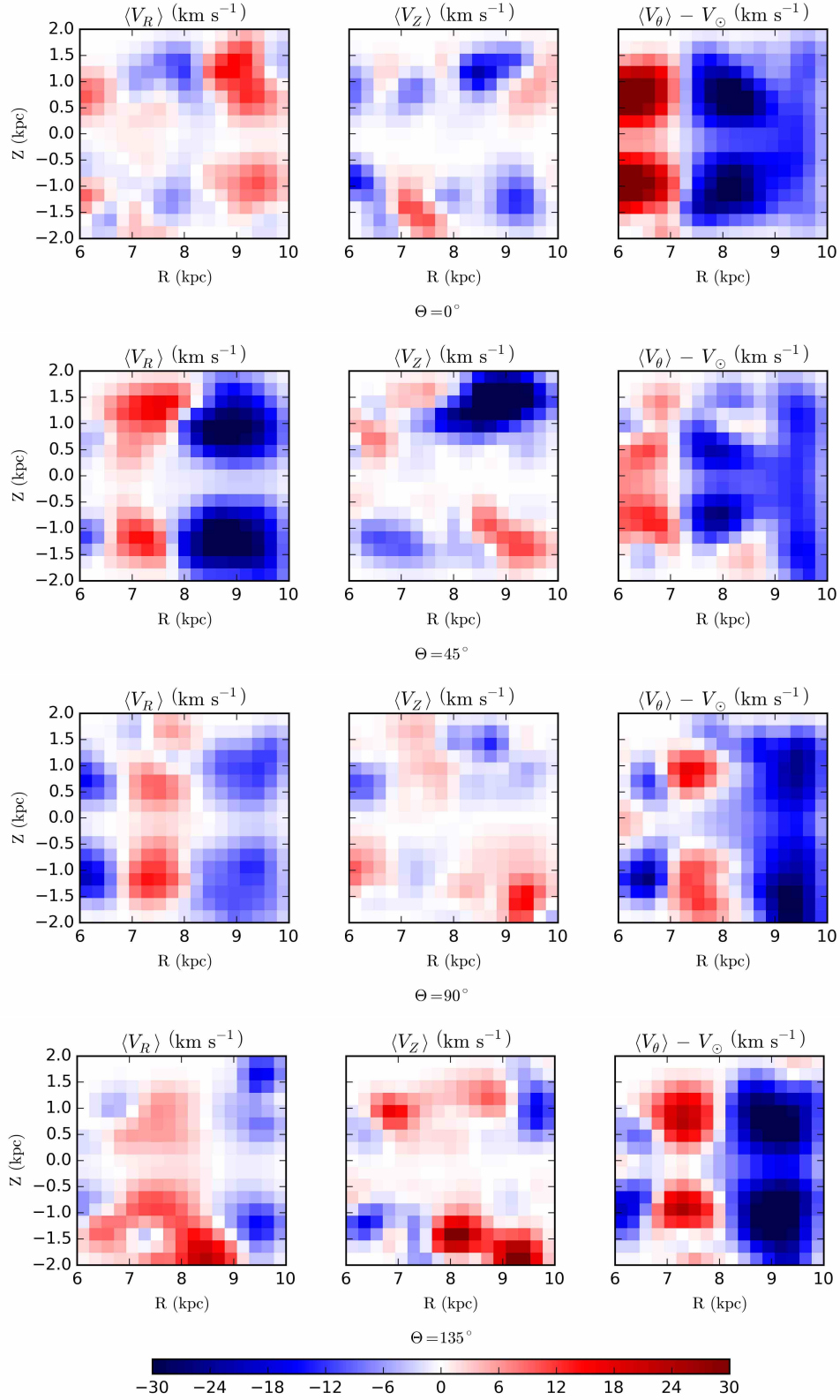


Figure 8. Mock observations of mean velocity components in local regions as a function of R and Z for simulation E1. Each row shows (from left to right) $\langle V_R \rangle$, $\langle V_Z \rangle$, and $\langle V_\theta \rangle - V_{\text{circ}}(R)$. Mean velocities have been extracted at different azimuth angles. Panels from top to bottom have central angle $\Theta = 0, 45, 90$ & 135° , respectively. The $\langle V_Z \rangle$ panel at $\Theta = 45^\circ$ displays a particularly large gradient.

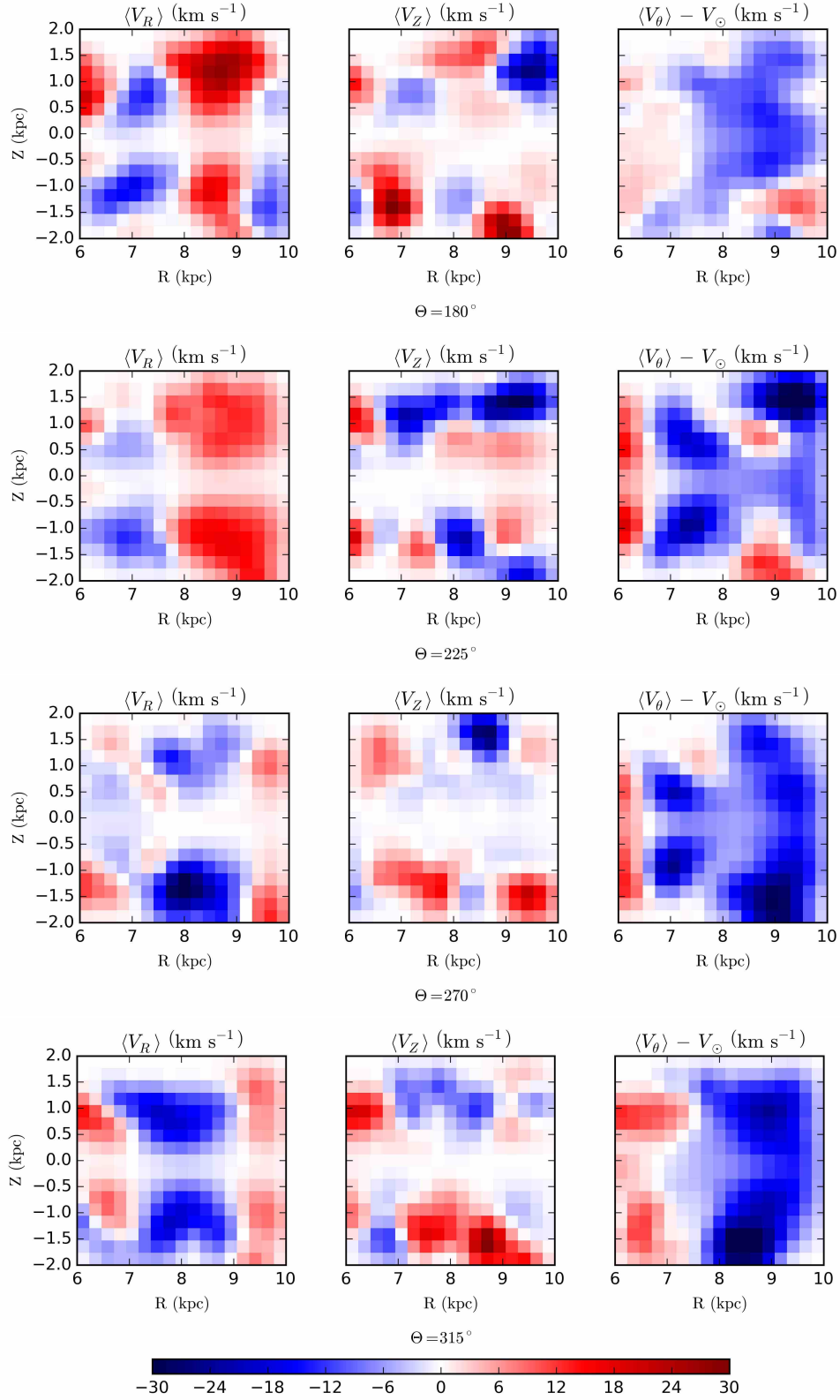


Figure 8. Figure 8 continued, with (top to bottom) $\Theta = 180, 225, 270$ & 315° .

it passes through the Galactic plane. For a star at \mathbf{x}_{s0} and velocity \mathbf{v}_s a linear trajectory $\mathbf{x}_s(t) = \mathbf{x}_{s0} + \mathbf{v}_s(t - t_0)$. These linear trajectories are those in the vicinity of the encounter, ignoring the gravitational interaction during encounter and the background Galactic potential, and we only use them to compute the velocity perturbations. In the frame with relative velocity $\mathbf{V} = \mathbf{v}_d - \mathbf{v}_s$ centered on the dwarf galaxy, the linear trajectory of the star is $\mathbf{x}_{s,com} = \mathbf{x}_{s0} - \mathbf{x}_{d0} - \mathbf{V}(t - t_0)$. By minimizing distance to the dwarf we find that the star (on the linear trajectory) is closest to the dwarf galaxy at time $t_{min} = t_0 + \mathbf{V} \cdot (\mathbf{x}_{s0} - \mathbf{x}_{d0})V^{-2}$. At this time the star is at

$$\mathbf{x}_{s,com}(t_{min}) = \mathbf{x}_{s0} - \mathbf{x}_{d0} - \mathbf{V} [\mathbf{V} \cdot (\mathbf{x}_{s0} - \mathbf{x}_{d0})] V^{-2}.$$

The vector between dwarf and star (and pointing toward the dwarf for the linear trajectory at closest approach) is the equivalent to this but with opposite direction

$$\mathbf{b} = \mathbf{x}_{d0} - \mathbf{x}_{s0} + \mathbf{V} [\mathbf{V} \cdot (\mathbf{x}_{s0} - \mathbf{x}_{d0})] V^{-2}$$

The length of \mathbf{b} is the impact parameter, b . The direction of \mathbf{b} gives the perpendicular direction for the velocity change (equation A1). The parallel velocity perturbation (equation A2) is in the direction of the relative velocity vector $-\hat{\mathbf{V}}$ with unit vector $\hat{\mathbf{V}} = (\mathbf{v}_d - \mathbf{v}_s)/|\mathbf{v}_d - \mathbf{v}_s|$. Rewriting equations A1 and A2, we can write the total velocity perturbation of the star as

$$\Delta \mathbf{v} = \frac{2bV^3}{GM(b)} \hat{\mathbf{b}} \left(1 + \frac{b^2V^4}{G^2M(b)^2} \right)^{-1} - 2V\hat{\mathbf{V}} \left(1 + \frac{b^2V^4}{G^2M(b)^2} \right)^{-1} \quad (\text{A3})$$

with first term the perpendicular component and the second term the parallel component. Here $\hat{\mathbf{b}}$ is the unit vector with the direction of \mathbf{b} . We approximate the dwarf galaxy mass as that integrated out to the impact parameter, $M(b)$ to take into account the spatial extent of the dwarf galaxy and to limit the size of the perturbations at small impact parameters. A Hernquist mass model (mass interior to radius r)

$$M(r) = M_d \frac{r^2}{(r + a_H)^2} \quad (\text{A4})$$

is used to model mass distribution of the dwarf galaxy, with Hernquist scale length $a_H = 3$ kpc. The scale length of the dwarf galaxy truncates the size of the largest velocity perturbations. However, as large perturbations are only induced over a very small area, the velocities for most of the perturbed disc are insensitive to the value of a_H used.

We restrict the effect of the hyperbolic approximation to stars within 18 kpc of the location of impact (the positions given in Table 1). Impact parameters larger than this (such as those for stars on the opposite side of the disc) would not be strongly perturbed by the encounter and the perturbations would not be well approximated by the instantaneous hyperbolic orbit approximation.

In the limit of high velocity or $b^2V^4/(GM(b))^2 \gg 1$ equation A3 becomes

$$\Delta \mathbf{v} = \hat{\mathbf{v}} \frac{2GM(b)}{bV} \quad (\text{A5})$$

resembling the impulse approximation for a point mass of

mass $M(b)$. For large impact parameter, $b \gg a_H$, the enclosed mass $M(b) \sim M_d$ and

$$\Delta \mathbf{v} \approx \hat{\mathbf{b}} \frac{2GM_d}{bV}$$

as would be expected for the impulse approximation for a point mass of mass M_d . The impulse approximation (Spitzer 1958; Cincotta et al. 1991) adopts a straight line for the trajectory of the perturber (here the dwarf galaxy), with respect to a star in the disk. The velocity perturbation of the star caused by an extended potential perturber (rather than a point mass) can be computed as

$$\Delta \mathbf{v} \approx \int_{-\infty}^{\infty} dt \nabla \Phi(t) \quad (\text{A6})$$

(Cincotta et al. 1991) where $\Phi(t)$ is the potential of the perturber on a linear trajectory. This can be integrated analytically for the Plummer model (Cincotta et al. 1991). Using the Hernquist gravitational potential, $\Phi(r) = -GM_d/(r + a_H)$, consistent with equation A4, equation A6 gives

$$\Delta \mathbf{v} \approx \hat{\mathbf{b}} \frac{2GM_d}{Vb} g(a_H/b) \quad (\text{A7})$$

with function

$$g(u) = \int_0^\infty \frac{dx}{(\sqrt{x^2 + 1} + u)^2 \sqrt{x^2 + 1}}.$$

In the limit of $b \gg a_H$, the limit $\lim_{u \rightarrow 0} g(u) = 1$ and we recover the impulse approximation for point mass $M = M_d$, consistent with the total enclosed perturber mass at large radius.

How accurate is equation A5 compared to equation A7? Computing the ratio of the two expressions at $b = a_H$ we find that equation A5 underestimates $|\Delta \mathbf{v}|$ by 30%. This underestimate is due to the neglect of the mass outside of radius $r = b$ in equation A5. Drawing from this computation, we estimate that we underestimate the velocity perturbation at $b = a_H$ using the hyperbolic orbit approximation (equation A3) by about the same fraction. For our two encounters most stars have impact parameters larger than a_H so we do not expect this underestimate to significantly influence our results.